

POPoS: Improving Efficient and Robust Facial Landmark Detection with Parallel Optimal Position Search

Chong-Yang Xiang^{1,5}, Jun-Yan He², Zhi-Qi Cheng³, Xiao Wu^{1,5}, Xian-Sheng Hua⁴

¹ Southwest Jiaotong University

² Institute for Intelligent Computing, Alibaba Group, China

³ Carnegie Mellon University

⁴ Terminus Labs, Terminus Group, China

⁵ Engineering Research Center of Sustainable Urban Intelligent Transportation, Ministry of Education, China

Abstract

Achieving a balance between accuracy and efficiency is a critical challenge in facial landmark detection (FLD). This paper introduces the Parallel Optimal Position Search (POPoS), a high-precision encoding-decoding framework designed to address the fundamental limitations of traditional FLD methods. POPoS employs three key innovations: (1) Pseudo-range multilateration is utilized to correct heatmap errors, enhancing the precision of landmark localization. By integrating multiple anchor points, this approach minimizes the impact of individual heatmap inaccuracies, leading to robust overall positioning. (2) To improve the pseudo-range accuracy of selected anchor points, a new loss function, named multilateration anchor loss, is proposed. This loss function effectively enhances the accuracy of the distance map, mitigates the risk of local optima, and ensures optimal solutions. (3) A single-step parallel computation algorithm is introduced, significantly enhancing computational efficiency and reducing processing time. Comprehensive evaluations across five benchmark datasets demonstrate that POPoS consistently outperforms existing methods, particularly excelling in low-resolution scenarios with minimal computational overhead. These features establish POPoS as a highly efficient and accurate tool for FLD, with broad applicability in real-world scenarios. The code is available at <https://github.com/teslatasy/POPoS>.

Introduction

Facial Landmark Detection (FLD) is a fundamental cornerstone in the field of computer vision, playing an indispensable role in the accurate identification and localization of salient facial features such as eye regions, nasal structures, and mouth contours in digital images. This crucial task underpins a wide range of advanced applications, including sophisticated facial recognition systems (Cheng et al. 2019; Huang et al. 2020b; Cheng et al. 2022; Liu et al. 2023), intricate three-dimensional face modeling techniques (Tu et al. 2023; Zhou et al. 2023a), and critical advances in autonomous vehicle technologies (Kim et al. 2023; Ghoddoosian, Galib, and Athitsos 2019). The importance of FLD extends far beyond mere detection; it serves as the linchpin for interpreting and analyzing human facial expressions,

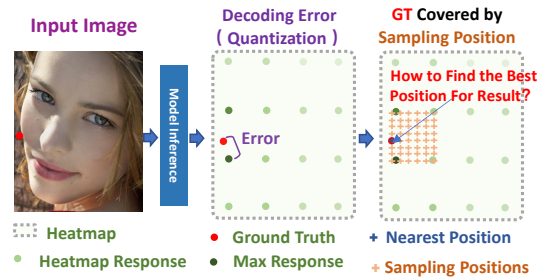


Figure 1: Visualization of quantization error in the coordinate decoding process. The discrepancy between the ground truth (GT) coordinates and the point of highest probability in the heatmap illustrates the challenge of achieving lossless decoding and precise localization.

emotional states, and identity markers in digital environments, catalyzing innovation in fields as diverse as human-computer interaction paradigms, augmented reality systems, and medical diagnostic protocols.

The advent of deep learning methods has brought about a paradigm shift in FLD research, primarily through two dominant approaches: heatmap-based methods and coordinate regression techniques. Heatmap regression methods (Chandran et al. 2020; Zhang et al. 2020; Jin, Liao, and Shao 2021) have received considerable attention due to their ability to generate probabilistic heatmaps for individual landmarks, effectively preserving spatial and contextual information while mitigating the risk of overfitting during the training process. These methods are remarkably effective at capturing the inherent uncertainty associated with landmark positions, providing robust performance across a wide range of facial expressions and orientations.

Despite their merits, heatmap-based approaches are not without challenges. One significant obstacle is the occurrence of quantization errors, particularly when downscaling heatmaps from their original resolution (Bao et al. 2023). This problem arises from the inevitable discretization of continuous spatial information into pixelated representations, resulting in a potential degradation of precision during the landmark localization process. While maintaining high-resolution heatmaps can partially mitigate this problem, it imposes significant computational requirements, making it impractical for real-time applications or deployment on resource-constrained devices.

The heart of the challenge in FLD is therefore to achieve an optimal balance between high-resolution accuracy and computational efficiency. This delicate balance becomes particularly critical in scenarios requiring real-time performance or in environments characterized by limited processing power. Although seminal works such as Hourglass (Newell, Yang, and Deng 2016), Crossnet (Zhang et al. 2022), and KeyposS (Bao et al. 2023) have made significant progress in addressing accuracy degradation in low-resolution heatmaps, the pursuit of an optimal trade-off between accuracy and efficiency remains an open challenge in the field. State-of-the-art methods often struggle to maintain high accuracy when faced with low-resolution heatmaps or stringent computational constraints.

This persistent challenge underscores the imperative for innovative encoding and decoding techniques that can overcome the inherent limitations of current paradigms. The research community is actively exploring novel approaches that leverage the strengths of heatmap-based methods while addressing their shortcomings, potentially through the development of hybrid architectures or advanced post-processing strategies. Fig. 1 illustrates a fundamental challenge in FLD: the quantization error inherent in the coordinate decoding process. This visual representation delineates the potential misalignment between the ground truth (GT) landmark coordinates and the point of highest probability as indicated by the heatmap. This discrepancy is a direct consequence of the discretization process, wherein the continuous spatial domain is mapped onto a discrete pixel grid, potentially compromising localization accuracy. The figure serves as a compelling argument for the necessity of sophisticated decoding strategies capable of bridging the gap between discretized heatmap representations and the continuous spatial domain of facial features.

To address these multifaceted challenges, we propose the Parallel Optimal Position Search (POPoS) framework, a novel approach designed to overcome the accuracy-efficiency trade-offs inherent in heatmap-based methods. POPoS introduces a series of innovative strategies that collectively address the core limitations of traditional FLD approaches. At its core, POPoS employs a pseudo-range multilateration technique that uses the top K points of the heatmap as anchors, effectively mitigating the impact of multiple peaks and ensuring accurate landmark localization. This is complemented by a specialized anchor-based optimization strategy that balances global and local optimization, compensating for quantization errors and improving sub-pixel accuracy. Furthermore, POPoS implements a single-step parallel computation algorithm that dramatically reduces computation time while maintaining high accuracy, making it particularly well-suited for modern GPU architectures. These improvements enable POPoS to demonstrate particular efficacy in low-resolution heatmaps scenarios without compromising on accuracy or computational efficiency, achieving an optimal balance between precision and efficiency. This positions POPoS as a viable solution for a wide spectrum of real-world applications, from mobile devices to advanced real-time systems. The key contributions of POPoS are:

- A novel pseudo-range multilateration approach that outperforms traditional methods in scenarios with multiple local maxima or ambiguous heatmap regions.
- An anchor-based optimization strategy that synergistically balances global and local optimization, enhancing sub-pixel accuracy.
- A GPU-optimized, single-step parallel computation algorithm that significantly improves efficiency over traditional iterative methods.
- Extensive evaluation across multiple benchmarks, demonstrating superior performance in low-resolution scenarios with minimal computational overhead.

Related Work

Facial landmark recognition has advanced through two key approaches: heatmap regression and high-efficiency heatmap decoding.

Heatmap Regression-Based Methods

Heatmap regression methods (Chandran et al. 2020; Sun et al. 2019; Tang et al. 2018; Zou et al. 2019; Wang, Bo, and Li 2019; Jin, Liao, and Shao 2021) have evolved to predict landmarks using high-resolution feature maps with increasing sophistication. The Stacked Hourglass Network (Newell, Yang, and Deng 2016) and UNet (Ronneberger, Fischer, and Brox 2015) established the foundation by preserving spatial relationships. Subsequent innovations addressed specific challenges: UDP (Huang et al. 2020a) tackled discretization errors, G-RMI (Papandreou et al. 2017) mitigated quantization errors by combining dense heatmaps with keypoint offsets, and the DSNT layer (Nibali et al. 2018) introduced coordinate supervision regularization. PIPNet (Jin, Liao, and Shao 2021) further streamlined the process with simultaneous predictions on low-resolution feature maps. This progression has consistently enhanced accuracy by leveraging spatial pixel relationships.

High Efficiency Heatmap Decoding Methods

While heatmap regression improved prediction accuracy, extracting coordinates from estimated heatmaps remained a critical area for optimization. High-efficiency decoding methods emerged to address this challenge. Darkpose (Zhang et al. 2020) refined heatmap generation and distribution analysis, while FHR (Tai et al. 2019) enhanced precision through improved fractional part estimation. Sub-pixel heatmap regression (Bulat, Sanchez, and Tzimiropoulos 2021) increased accuracy by predicting offsets using soft continuous maximum values. KeyPosS (Bao et al. 2023) introduced a novel approach by integrating GPS-inspired true-range multi-point positioning technology.

Building on these advancements, our Parallel Optimal Position Search (POPoS) method combines pseudo-range multilateration with Potential Position Parallel Sampling. POPoS addresses limitations in predictive accuracy and computational efficiency, particularly at lower heatmap resolutions. This innovation not only advances facial landmark detection but also extends its applicability to resource-constrained environments, marking a significant step to-

wards more accessible and efficient high-accuracy detection across diverse applications and hardware configurations.

Parallel Optimal Position Search (POPoS)

Despite advancements like HRNet (Sun et al. 2019), heatmap-based facial landmark detection faces persistent challenges. Given an input image $I \in \mathbb{R}^{H \times W \times 3}$, the objective is to locate N_k facial landmarks $\{\beta_k\}_{k=1}^{N_k}$, where $\beta_k = (u_k, v_k)$. Current approaches use CNNs to generate heatmaps $\mathcal{H} \in \mathbb{R}^{h \times w \times N_k}$, with $h = H/\lambda$, $w = W/\lambda$, and λ as the downsampling factor. Key challenges include:

- **Resolution-Efficiency Trade-off.** High-resolution heatmaps ($\lambda \rightarrow 1$) provide precise localization but increase computational load, hindering real-time performance (Newell, Yang, and Deng 2016). Low-resolution heatmaps ($\lambda \gg 1$) are efficient but less accurate, impacting applications in resource-constrained scenarios.
- **Encoding-Decoding Dilemma.** Biased encoding ($\beta_{\text{biased}} = \text{Quan}(\beta/\lambda)$) introduces quantization errors, especially at large λ (Zhang et al. 2020). Unbiased encoding ($\beta_{\text{unbiased}} = \beta/\lambda$) maintains accuracy but results in diffuse heatmaps and increased computational cost (Zhang et al. 2020).
- **Decoding Limitations.** One-hot decoding ($\hat{\beta} = \text{argmax}(\mathcal{H})$) is efficient but prone to discretization errors. Distribution-aware methods (Zhang et al. 2020) perform well at high resolutions but struggle with low-resolution or multi-modal heatmaps, particularly in complex scenarios (Chandran et al. 2020).
- **Optimization Constraints.** The commonly used Mean Squared Error (MSE) loss assumes Gaussian error distribution, often inappropriate for facial landmarks (Zhang et al. 2020). It fails to capture spatial relationships between landmarks, leading to anatomically implausible configurations.

These interconnected challenges hinder robust, accurate, and efficient facial landmark detection across diverse scenarios. To address these challenges, we propose Parallel Optimal Position Search (POPoS), a novel framework that fundamentally reimagines heatmap-based facial landmark detection. POPoS comprises three stages, as illustrated in Fig. 2. First, the model optimization phase involves the generation of heatmaps and optimization, where the multilateration anchor loss is conducted to reduce encoding information loss. Second, the heatmap generation and anchor sampling phase include model inference, distance transformation, and anchor point selection. Third, the sample and search phase involves constructing the pseudo-range positioning equation, parallel sampling, and equivalent single-step parallel computation.

Model & Optimization

Our adopted HRNet (Bao et al. 2023), specially optimized for memory efficiency, is particularly suitable for mobile and edge computing applications. Its optimizations include early downsampling and a consistent application of 3×3 convolutional kernels, ensuring a balance between performance and

computational efficiency. The optimization objective of current Mean Squared Error (MSE) loss is to minimize the average squared difference between the predicted values and the actual values of the entire heatmap. While the predicted values often biased towards outliers at low resolutions after optimization, which will induce encoding errors. To enhance accuracy of the distance map for anchor points during the decoding step, the inconsistent optimization objectives between the decoding and encoding steps need to be solved. The Multilateration Anchor (MA) loss (Eq.1) is proposed to address the optimization challenge by enhancing accuracy within the top K points, where top K points correspond to the K station anchors at the decoding step:

$$\mathcal{L}_{\text{MA}} = \sum_{i=1}^{N_k} \|\mathcal{H}_i \cdot \text{Mask}_i - \hat{\mathcal{H}}_i \cdot \text{Mask}_i\|_2, \quad (1)$$

where \mathcal{H}_i and $\hat{\mathcal{H}}_i$ are the ground truth and predicted heatmaps, and $\text{Mask}_i \in \mathbb{R}^{h \times w}$ indicates a binary mask which assigns the top K response locations with value one, while the others remain zero, i represents the i -th landmark.

Further, the model is jointly optimized using MSE loss and MA loss. The loss L in the training stage is $L = \mathcal{L}_{\text{MSE}} + w \times \mathcal{L}_{\text{MA}}$, where \mathcal{L}_{MSE} is the MSE loss of the whole heatmap, \mathcal{L}_{MA} is the MA loss, and w is the weight parameter of local anchor loss.

Heatmap Generation & Anchor Sampling

In this stage, there are three key steps: heatmap generation, distance transformation, and anchor sampling.

First step is heatmap generation: An input image $I \in \mathbb{R}^{H \times W \times 3}$ is processed through a streamlined HRNet variant (Bao et al. 2023) to extract features. The heatmaps $\mathcal{H} \in \mathbb{R}^{h \times w \times N_k}$ is then generated, where $h = H/\lambda$, $w = W/\lambda$, and N_k represents the number of facial landmarks. The unbiased coordination encoding is employed during the encoding stage. The coordinate heatmap is generated as a 2-dimensional Gaussian distribution/kernel centered at the labeled coordinate.

The second step is distance transformation, which converts the heatmap into a distance map. The distance between the predicted position and each heatmap pixel, $\mathcal{D}(i, j)$, is calculated as $\mathcal{D}(i, j) = \sqrt{-2\sigma^2 \ln(\mathcal{H}(i, j))}$, where σ is the standard deviation of the Gaussian distribution. Because the heatmap retains the initial positional information entirely, thereby the distance heatmap maintains sub-pixel accuracy.

The second step is anchor sampling. To mitigate the influence of prediction errors induced by heatmap generation, different from the triangulation algorithm (Tai et al. 2019), the top K points of the distance map are selected as anchors. Because the selected top K points are consistent with those top K points in the model optimization stage, they promise to minimize information loss. Meanwhile, these selected top K points are utilized to form distance equations in the next stage.

Parallel Sampling & Computing

This stage involve two steps, forming pseudo-range multi-lateration equation, potential position parallel sampling and

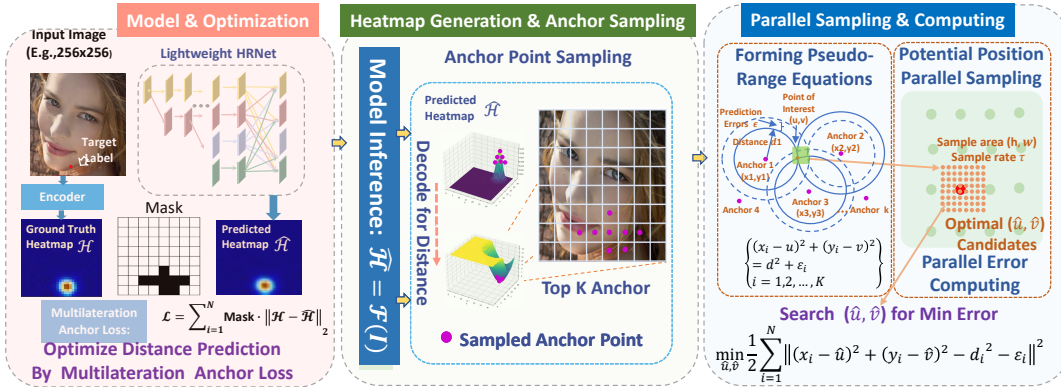


Figure 2: Parallel Optimal Position Search (POPoS) framework. The Multilateration Anchor Loss is designed during the training phase to optimize distance prediction. During model inference, POPoS samples the top-K response positions as anchor points for distance map decoding.

computing.

Forming Pseudo-range Multilateration Equations The distance map decoding is treated as the pseudo-range multilateration (PRM) problem. Here we utilize selected top K points as anchors, to form a set of distance equations. These distance equations represent the distances between multiple station anchors with the target point. Formally, the top K anchors are $\mathcal{A} = \{A_{(x_0, y_0)}, \dots, A_{(x_K, y_K)}\}$, the real distances between \mathcal{A} and the real position point of interest $\beta(u, v)$ are $\mathcal{D} = \{d_0, \dots, d_K\}$, and the prediction distance error for each anchor is denoted by ε_i . The system of non-linear PRM equations is given by Eq. 2:

$$\{(x_i - u)^2 + (y_i - v)^2 = d_i^2 + \varepsilon_i \mid i = 0, 1, \dots, K\}. \quad (2)$$

Potential Position Parallel Sampling and Computing To solve the pseudo-range multilateration equation and find the point of interest $\hat{\beta} = (\hat{u}, \hat{v})$, the objective function is constructed as Eq. 3:

$$\min_{\hat{u}, \hat{v}} \frac{1}{2} \sum_{i=1}^K \left\| (x_i - \hat{u})^2 + (y_i - \hat{v})^2 - d_i^2 - \varepsilon_i \right\|^2, \quad (3)$$

where ε_i represents the error between the decoded distance and the actual distance.

A novel method for solving the objective function is proposed, called Potential Position Parallel Sampling and Computing (PPPSC). Through three steps (potential region selection, candidate generation, and Solution of Parallel Computing), it can directly find the point that minimizes the objective function.

Potential Region Selection. First, considering the subpixel scenario, there are an infinite number of points existing in the heatmap. Second, as the distance between the sample point with the maximum value point m in the heatmap increases, the probability of sampling point hitting the point of interest decreases. Third, an excess of sampling can lead to redundant computations. Hence, the search area is set as a square region of $h \times w$ centered at point m .

Candidates Generation. Within the selected region, sampling is conducted using a mesh with a frequency of τ samples per pixel and obtained a total of N points. Formally, a

mesh grid point set $G = \{g_1, \dots, g_N\}$ is generated first, $g_i = (\frac{\Delta \hat{u}_i}{\lambda}, \frac{\Delta \hat{v}_i}{\lambda})$, where $\Delta \hat{u}_i \in [0, \lambda \times h \times \tau]$, $\Delta \hat{v}_i \in [0, \lambda \times w \times \tau]$. And τ is a factor to control the granularity of subpixel sampling. λ is the downsampling factor. Then, the mesh grid point set G is translated to cover the maximum value position (\hat{u}_m, \hat{v}_m) in the grid center, and the candidates $c_i \in C$ is computed as Eq. 4:

$$c_i(\hat{u}_i, \hat{v}_i) = \left(\frac{\Delta \hat{u}_i}{\lambda} + \hat{u}_m - \frac{w}{2}, \frac{\Delta \hat{v}_i}{\lambda} + \hat{v}_m - \frac{h}{2} \right). \quad (4)$$

Solution of Parallel Computing.

After the sampling, the computing step for one heatmap is formed as Eq. 5. All points from the sampling set C are then inputted into the objective function $\Phi(\mathcal{A}, C)$, which calculates the discrepancy between two distance matrices: one is the Euclidean distance matrix between the sampled points C and the anchor set \mathcal{A} , and the other one is the predicted distance map D of anchor set \mathcal{A} . This results in an error matrix E . The optimal facial landmark position is determined by locating the minimum position index in the matrix E .

$$\begin{aligned} \Phi(\mathcal{A}, C) &= \arg \min_i \sum_k (||C - A||_2 - D)_{ik} \\ &= \min_{\hat{u}, \hat{v}} \sum_{i=1}^K \left\| (x_i - \hat{u})^2 + (y_i - \hat{v})^2 - d_i^2 - \varepsilon_i \right\|^2, \end{aligned} \quad (5)$$

where x_i and y_i are the coordinates of the i -th anchor point. \hat{u} and \hat{v} are the coordinates of the sampled point, d_i is the measured distance from anchor i to the target point, ε_i represents error between the decoded distance and the actual distance for the i -th anchor. The optimization objectives of Eq. 3 and Eq. 5 are consistent, thus PPPSC methods can achieve the optimal approximate solution.

At last, Iterative Gauss–Newton Optimization (IGNO) for PRM is introduced. To validate the effectiveness of our approach, we implemented a general method, IGNO, for solving nonlinear equations of the PRM. Specifically, we utilized the Gauss–Newton iteration method to solve the PRM objective function Eq. 3. To find the point of interest $\hat{\beta} = (\hat{u}, \hat{v})$, the iteration starts at some initial guess $\hat{\beta}_0$, and update $\hat{\beta}_{n+1} = \hat{\beta}_n + \Delta \hat{\beta}$. At each iteration, the update $\Delta \hat{\beta}$ can

be calculated from Eq. 6:

$$\left(\sum_{i=1}^k \mathbf{J}_i^{-1} \mathbf{J}_i^T \right) \Delta \hat{\beta} = \sum_{i=1}^k -\mathbf{J}_i^{-1} e_i, \quad (6)$$

where k represents the number of anchors, \mathbf{J} is Jacobian matrix of the objective function, e_i represents the objective function value at the i -th iteration. The iteration process halts either when e_i gradually converges or when it reaches the upper limit of iterations. The IGNO methods require computations for each point individually, which has some challenges such as extensive loop operations and GPU acceleration. The proposed PPPSC approach only involves matrix operations, and is thus inherently suitable for parallel computation on GPUs. The computational complexity of the PPPSC approach can be expressed as $4 \times N_a \times N_c$, where N_a represents the number of anchors in \mathcal{A} , and N_c is the number of samples in C . While, IGNO’s complexity, which requires multiplicative operations and matrix-solving computations, is larger than $(24 \times N_a + 30) \times N_{iter}$, where N_{iter} is the iteration count. The PPPSC enables parallel operations on the heatmaps within a batch, and facilitates parallel processing on both the encoding and decoding steps on the GPU. The PPPSC’s complexity is much less than IGNO’s. The following experiment result in Table 2 also prove this conclusion.

Experiments

Dataset and Metric

Datasets Five landmark detection datasets are employed for a comprehensive evaluation of the POPoS framework:

- **COFW** (Artizzu, Perona, and Dollár 2013) comprises 1,345 training and 507 testing images, each with 29 annotated landmarks. This dataset emphasizes scenes with faces under occlusion.
- **AFLW** (Köstinger et al. 2011) includes a diverse set of approximately 25,000 face images from Flickr, annotated with up to 21 landmarks per image, showcasing wide variations in appearance and environmental conditions.
- **COCO-WholeBody** (Jin et al. 2020) offers a collection of over 200,000 labeled images and 250,000 instances across 133 keypoint categories, including comprehensive annotations for face landmarks.
- **300W** (Sagonas et al. 2016) consists of approximately 3,937 face images, each annotated with 68 facial landmarks, encompassing a broad spectrum of identities, expressions, and lighting conditions.
- **WFLW** (Wu et al. 2018) is a widely-used dataset in facial landmark detection, containing 10,000 images (7,500 for training, 2,500 for testing), that each image is annotated with 98 landmarks.

Evaluation Metric. Following standard practice in facial landmark detection (Bao et al. 2023), the Normalized Mean Error (NME) is used as evaluation metric, which is defined as $\frac{1}{N_k} \sum_{i=1}^N \frac{\|\beta_i - \hat{\beta}_i\|_2}{d}$, where N_k is the number of landmarks, β and $\hat{\beta}$ represent the ground truth and predicted landmarks, respectively, and d is the normalization factor, typically the interpupillary distance.

Table 1: Comparison with the State-of-the-Art methods. The results are in NME (%). The best results are highlighted with bold text font. * means the result of IGNO solution.

Method	WFLW	300W	AFLW	COFW	Para.	GFlops
TSR (Lv et al. 2017)	-	4.99	2.17	-	-	-
Wing (2018)	-	3.60	1.47	-	91.0M	5.5
ODN (2019)	-	4.17	1.63	5.30	-	-
DeCaFa (2019)	4.62	3.39	-	-	10M	-
DAG (2020)	4.21	3.04	-	4.22	-	-
AWing (2019)	4.36	3.07	1.53	4.94	24.1M	26.7
AVS (2019)	4.39	3.86	1.86	4.43	28.3M	2.4
ADA (2020)	-	3.50	-	-	-	-
LUVLi (2020)	4.37	3.23	1.39	-	-	-
PIPNet-18 (Jin, Liao, and Shao 2021)	4.57	3.36	1.48	-	12.0M	2.4
PIPNet-101 (Jin, Liao, and Shao 2021)	4.31	3.19	1.42	-	45.7M	10.5
DTLD (Li et al. 2022a)	4.08	2.96	1.38	-	-	-
RePFormer (Li et al. 2022b)	4.11	3.01	1.43	-	-	-
SLPT (Xia et al. 2022)	4.14	3.17	-	-	9.98M	-
EF-3-ACR (Fard and Mahoor 2022)	-	3.75	-	3.47	-	-
ADNet-FE5 (Huang et al. 2023)	4.1	2.87	-	-	-	-
ResNet50-FE5 (Huang et al. 2023)	-	4.39	-	-	-	-
HRNet-FE5 (Huang et al. 2023)	-	3.46	-	-	-	-
STAR Loss (Zhou et al. 2023b)	4.02	2.87	-	4.62	13.37M	-
RHT-R (Wan et al. 2023)	4.01	3.46	1.99	4.42	-	-
POPos (ours, 32 ²)	4.28	3.38	1.43	3.8	9.7M	1.2
POPos (ours, 64 ²)	3.95*	3.28*	1.34	3.44	9.7M	4.7

Table 2: FPS of existing decoding methods and PoPoS

	FPS	Cost
One-hot	2819	0.36ms
Two-hot (Newell, Yang, and Deng 2016)	1394	0.72ms
DarkPose (Zhang et al. 2020)	186.2	5.3ms
KeyPosS (Bao et al. 2023)	96.5	10.34ms
IGNO for PRM	2.5	405.06ms
POPoS	1301	0.76ms

Implementation Details

Our proposed POPoS framework builds upon the KeyPosS and MMpose¹ frameworks. Under same condition with KeyPosS’s preprocessing and augmentation techniques, we evaluate the performance at varying heatmap resolutions: 64 × 64, 32 × 32, 16 × 16, 8 × 8, and 4 × 4 pixels. The backbone network is a lightweight variant of HRNet (Sun et al. 2019), which is pre-trained on ImageNet (Russakovsky et al. 2015) and fine-tuned using the Adam optimizer (Kingma and Ba 2015) with a linear-step decay learning rate schedule. The initial learning rate is set at 2.0e-3, and gradually reducing to 1.0e-5 over 100 epochs. The training is performed on a 4 × NVIDIA 3090 GPU server, with a batch size aligned with KeyPosS (Bao et al. 2023).

Comparison with State-of-the-Art Methods

The effectiveness of the Parallel Optimal Position Search (POPoS) is evaluated against state-of-the-art methods across five pivotal datasets, detailed in Table 1. The NME of POPoS is less than the traditional coordinate regression-based method and other heatmap-based methods. We think

¹<https://github.com/open-mmlab/mmPose>

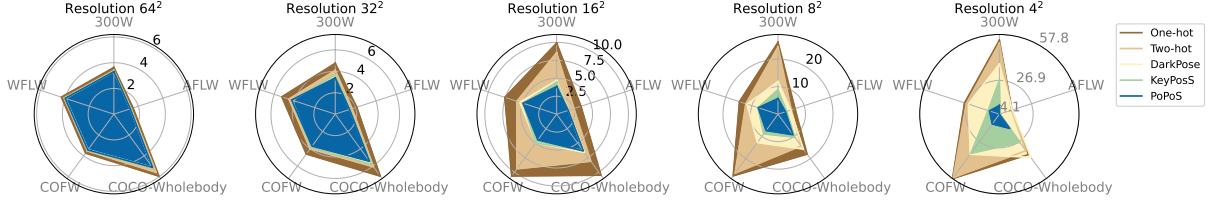


Figure 3: Keypoint detection accuracy at heatmap resolutions of 64×64 , 32×32 , 16×16 , 8×8 , and 4×4 . (The smaller radar map denotes the better performance)

that coordinate regression-based methods (TSR, Wing, et al) compromise spatial detail retention, thereby affecting precision in high-resolution scenarios. POPoS’s exceptional performance, particularly on the WFLW, AFLW, COFW, and COCO-Wholebody datasets, emphasizes its improved capability in addressing encoding and decoding errors.

Notably, POPoS achieves impressive performance in WFLW, AFLW, and COFW with fewer parameters and higher computational efficiency. On the 300W dataset, POPoS reaches a competitive result Normalized Mean Error (NME) of 3.28%, highlighting the complexity of the dataset and the challenges with limited training data. Notice that, the NME value of the COCO-Wholebody dataset is only used to analyze the decoding precious of various heatmap resolutions, as seen in Fig. 3.

Comparison with Current Decoding Schemes

The core problem addressed in this article is the verification of decoding accuracy at different resolutions. The decoding effects of five different methods were compared across five datasets under various heatmap resolution settings. As shown in Fig. 3, a distinctive advantage of POPoS is found in the integration of the Iterative Gauss–Newton Optimization (IGNO) approximation method with a strategic sampling approach. This integration is especially beneficial in low-resolution settings, where high-quality results are delivered efficiently by POPoS.

Additionally, to evaluate the efficiency of our proposed POPoS on heatmap decoding, the processing speed of different decoding methods, with the metric of Frame per second (FPS), is calculated. Although the current heatmap inference speed reaches 200 FPS (Jin, Liao, and Shao 2021), slow heatmap decoding could potentially become a bottleneck. The decoding speed of five methods, one-hot, two-hot, Dark (Zhang et al. 2020), KeyPosS (Bao et al. 2023), and POPoS are compared in Table 2. The FPS for 256×256 input images with 64×64 heatmaps was measured to assess decoding speed. It is clear that the POPoS is 15 times faster than KeyPos, 6 times faster than Dark (Zhang et al. 2020), and comparable in speed to Two-Hot. Although slower than One-Hot, POPoS has significantly improved accuracy and meets real-time processing requirements.

Ablation Studies

This part offer an in-depth analysis on the effect of the proposed modules and the hyperparameter settings.

Effect of Pseudo-Range Multilateration The efficacy of the Iterative Gauss–Newton Optimization (IGNO) for

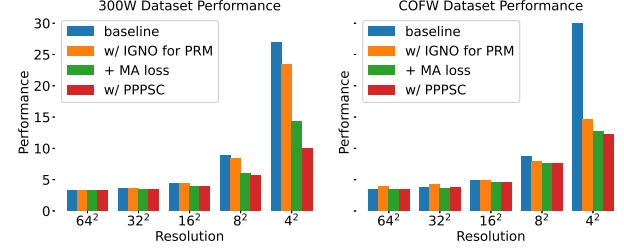


Figure 4: Effect of Gauss–Newton Optimization (IGNO), Multilateration Anchor (MA) loss, and Potential Position Parallel Sampling and Computing (PPPSC).

pseudo-range multilateration (PRM) was examined by integrating it into the baseline model, replacing the least squares approximation. Iterations were set to a maximum of 20 or terminated upon convergence. The KeyposS (Bao et al. 2023) was considered as the baseline. Notable improvements were observed in the 300W and COFW datasets as shown in Fig. 4. This outcome is attributed to a decrease in prediction errors with a larger number of anchors.

Effect of MA Loss The influence of Multilateration Anchor (MA) loss in addressing encoding errors was evaluated by retraining the HRNet network across various resolutions. The results showed significant improvements of the POPoS in all datasets when the multilateration anchor loss was integrated, as shown in Fig. 4. Specifically, in the 4×4 resolution heatmap, the prediction errors decreased by 47% for the 300W dataset and 58% for the COFW dataset.

Effect of PPPSC The Potential Position Parallel Sampling and Computing (PPPSC) is tested on five datasets at different resolutions, as shown in Fig. 4. This strategy notably bolstered the stability and performance of the IGN Optimization algorithm. For the ablation experiments on the parameter settings of sampling range (h, w) and sampling frequency τ , tests are conducted on the 300W dataset to evaluate the impact of different parameters on the experimental results at a resolution of 32×32 resolution heatmap. The experimental outcomes are illustrated in Fig. 5. Ablation studies on the sample area indicated that the optimal values are distributed within the range of 1–2 pixels around the maximum value. Increasing the sampling range does not improve decoding accuracy. This suggests that, for certain challenging samples, errors already exist during the model’s prediction phase, specifically in the encoding stage, and cannot be optimized by reducing decoding errors. Ablation studies on the sample rate τ indicated that optimal performance is attained with approximately 10 sampling points per pixel

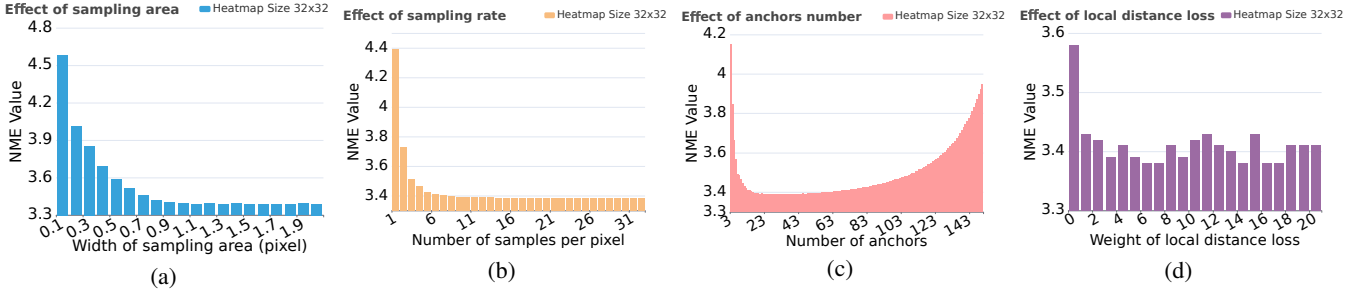


Figure 5: Detailed analysis of POPoS performance factors: (a) Effect of sampling area (b) Effect of sampling rate τ (c) Anchor number and (d) Local distance loss weight, each illustrating their impact on the accuracy of predictions

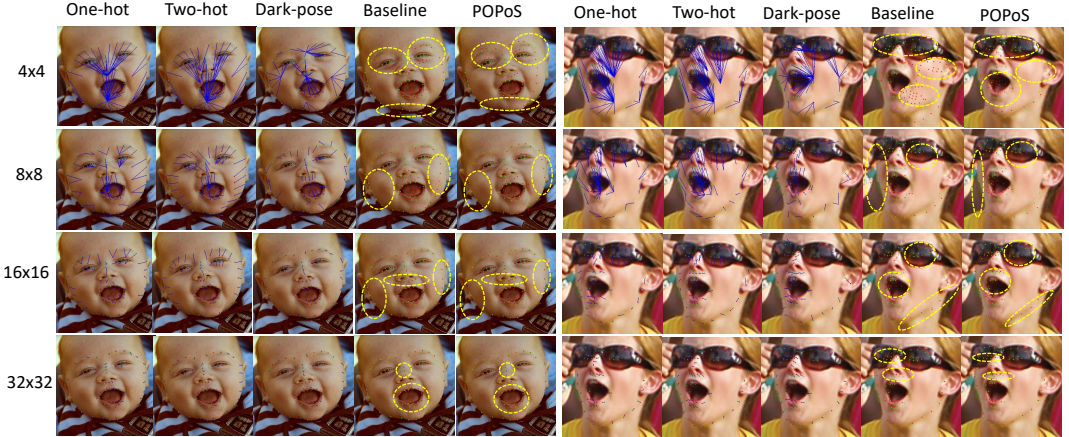


Figure 6: Visualization of POPoS's performance in low-resolution settings: Comparative analysis with one-hot, two-hot, dark-pose, and KeyPosS methods. Ground truth is represented by green dots, predictions by red dots, discrepancies by blue lines, and significant inaccuracies are circled in yellow. (Best viewed in color and at a higher zoom level.)

length, equating to about 1.2 points per original image pixel as shown in Fig. 5a. Further increasing the number of sampling points yielded negligible improvements.

Ablation study on hyperparameter settings The ablation study of anchor number N_a in the decoding step, as illustrated in the Fig. 5c indicating that too few anchor results in inaccurate predictions, while excessive anchor introduces larger calculation error. In the case of a 32×32 resolution heatmap, the optimal number of anchors is determined to be 25. An ablation experiment on the weight of the local anchor loss in the 300W dataset (Fig. 5d) demonstrated consistent improvement in prediction accuracy across various weight ratios, with the most effective being a ratio of 6. This finding underscores the critical impact of encoding accuracy errors on pseudo-range multilateration and the effectiveness of the local anchor loss in mitigating convergence issues.

Visualization Analysis

To evaluate POPoS's adaptability in practical applications, a comprehensive visualization analysis was conducted. The results were compared against traditional methods such as one-hot, two-hot, DarkPose, and KeyPosS. This comparison focused on challenging low-resolution scenarios, as depicted in Fig. 6. The analysis highlighted that traditional methods like one-hot, two-hot, and dark-pose struggle with precision at lower heatmap resolutions such as 4×4 and 8×8 . POPoS

shows superior performance at 4×4 and higher resolutions. Furthermore, POPoS consistently addresses localization errors across all examined resolutions. This proficiency is particularly evident in Fig. 6, where POPoS significantly outperforms the traditional methods.

The visualization confirms the robustness of POPoS, demonstrating its capability to optimize encoding and decoding errors effectively in diverse application scenarios.

Conclusion

In summary, a novel heatmap based method with accuracy-efficiency trade-offs named Parallel Optimal Position Search (POPoS) framework is built. In encoding stage, the multilateration anchor loss function is proposed, which reduce the prediction error of heatmap. In the decoding stage, an optimization-based multilateration method is employed, which overcomes accuracy constraints in traditional method. And the Equivalent Single-Step Parallel Computation algorithm is proposed to significantly enhance computational efficiency. Our testing results on five widely recognized datasets demonstrate that POPoS performs exceptionally well, particularly under low-resolution heatmap conditions. In general, POPoS achieves effect balance between accuracy and efficiency. This advancement demonstrates a significant leap forward in the facial landmark detection domain.

References

Artizzu, X. P. B.; Perona, P.; and Dollár, P. 2013. Robust Face Landmark Estimation under Occlusion. In *IEEE Int. Conf. Comput. Vis.*, 1513–1520.

Bao, X.; Cheng, Z.-Q.; He, J.-Y.; Xiang, W.; Li, C.; Sun, J.; Liu, H.; Liu, W.; Luo, B.; Geng, Y.; et al. 2023. KeyPosS: Plug-and-Play Facial Landmark Detection through GPS-Inspired True-Range Multilateration. In *ACM Int. Conf. Multimedia*, 5746–5755.

Bulat, A.; Sanchez, E.; and Tzimiropoulos, G. 2021. Sub-pixel Heatmap Regression for Facial Landmark Localization. In *Brit. Mach. Vis. Conf.*, 422.

Chandran, P.; Bradley, D.; Gross, M. H.; and Beeler, T. 2020. Attention-Driven Cropping for Very High Resolution Facial Landmark Detection. In *IEEE Conf. Comput. Vis. Pattern Recognit.*

Cheng, Z.-Q.; Dai, Q.; Li, H.; Song, J.; Wu, X.; and Hauptmann, A. G. 2022. Rethinking spatial invariance of convolutional networks for object counting. In *IEEE Conf. Comput. Vis. Pattern Recognit.*, 19638–19648.

Cheng, Z.-Q.; Li, J.-X.; Dai, Q.; Wu, X.; He, J.-Y.; and Hauptmann, A. G. 2019. Improving the Learning of Multi-column Convolutional Neural Network for Crowd Counting. In *ACM Int. Conf. Multimedia*, 1897–1906.

Dapogny, A.; Cord, M.; and Bailly, K. 2019. DeCaFA: Deep Convolutional Cascade for Face Alignment in the Wild. In *IEEE Int. Conf. Comput. Vis.*, 6892–6900.

Fard, A. P.; and Mahoor, M. H. 2022. ACR loss: Adaptive coordinate-based regression loss for face alignment. In *Int. Conf. Pattern Recognit.*, 1807–1814. IEEE.

Feng, Z.; Kittler, J.; Awais, M.; Huber, P.; and Wu, X. 2018. Wing Loss for Robust Facial Landmark Localisation With Convolutional Neural Networks. In *IEEE Conf. Comput. Vis. Pattern Recognit.*, 2235–2245.

Ghoddoosian, R.; Galib, M.; and Athitsos, V. 2019. A Realistic Dataset and Baseline Temporal Model for Early Drowsiness Detection. In *IEEE Conf. Comput. Vis. Pattern Recognit. (CVPR) Workshops*.

Huang, J.; Zhu, Z.; Guo, F.; and Huang, G. 2020a. The Devil Is in the Details: Delving Into Unbiased Data Processing for Human Pose Estimation. In *IEEE Conf. Comput. Vis. Pattern Recognit.*, 5699–5708.

Huang, S.; Li, X.; Cheng, Z.-Q.; Zhang, Z.; and Hauptmann, A. 2020b. Stacked pooling for boosting scale invariance of crowd counting. In *IEEE Int. Conf. Acoust. Speech Signal Process.*, 2578–2582. IEEE.

Huang, Y.; Chen, X.; Kim, J.; Yang, H.; Li, C.; Yang, J.; and Chen, D. 2023. FreeEnricher: Enriching Face Landmarks without Additional Cost. In *AAAI Conf. Artif. Intell.*, volume 37, 962–970.

Jin, H.; Liao, S.; and Shao, L. 2021. Pixel-in-Pixel Net: Towards Efficient Facial Landmark Detection in the Wild. *International Journal of Computer Vision*, (12): 3174–3194.

Jin, S.; Xu, L.; Xu, J.; Wang, C.; Liu, W.; Qian, C.; Ouyang, W.; and Luo, P. 2020. Whole-Body Human Pose Estimation in the Wild. In *Eur. Conf. Comput. Vis.*, volume 12354, 196–214.

Kim, D.; Park, H.; Kim, T.; Kim, W.; and Paik, J. 2023. Real-time driver monitoring system with facial landmark-based eye closure detection and head pose recognition. *Scientific reports*, 13(1): 18264.

Kingma, D. P.; and Ba, J. 2015. Adam: A Method for Stochastic Optimization. In *Int. Conf. Learn. Represent.*

Köstinger, M.; Wohlhart, P.; Roth, P. M.; and Bischof, H. 2011. Annotated Facial Landmarks in the Wild: A large-scale, real-world database for facial landmark localization. In *IEEE Int. Conf. Comput. Vis. Workshops*, 2144–2151.

Kumar, A.; Marks, T. K.; Mou, W.; Wang, Y.; Jones, M.; Cherian, A.; Koike-Akino, T.; Liu, X.; and Feng, C. 2020. LUVLi Face Alignment: Estimating Landmarks’ Location, Uncertainty, and Visibility Likelihood. In *IEEE Conf. Comput. Vis. Pattern Recognit.*, 8233–8243.

Li, H.; Guo, Z.; Rhee, S.; Han, S.; and Han, J. 2022a. Towards Accurate Facial Landmark Detection via Cascaded Transformers. In *IEEE Conf. Comput. Vis. Pattern Recognit.*, 4166–4175.

Li, J.; Jin, H.; Liao, S.; Shao, L.; and Heng, P.-A. 2022b. Repformer: Refinement pyramid transformer for robust facial landmark detection. *arXiv preprint arXiv:2207.03917*.

Li, W.; Lu, Y.; Zheng, K.; Liao, H.; Lin, C.; Luo, J.; Cheng, C.; Xiao, J.; Lu, L.; Kuo, C.; and Miao, S. 2020. Structured Landmark Detection via Topology-Adapting Deep Graph Learning. In *Eur. Conf. Comput. Vis.*, volume 12354, 266–283.

Liu, H.; Xiang, W.; He, J.-Y.; Cheng, Z.-Q.; Luo, B.; Geng, Y.; and Xie, X. 2023. Refined Temporal Pyramidal Compression-and-Amplification Transformer for 3D Human Pose Estimation. *arXiv preprint arXiv:2309.01365*.

Lv, J.; Shao, X.; Xing, J.; Cheng, C.; and Zhou, X. 2017. A Deep Regression Architecture with Two-Stage Re-initialization for High Performance Facial Landmark Detection. In *IEEE Conf. Comput. Vis. Pattern Recognit.*, 3691–3700.

Newell, A.; Yang, K.; and Deng, J. 2016. Stacked Hourglass Networks for Human Pose Estimation. In *European Conference on Computer Vision*, volume 9912, 483–499.

Nibali, A.; He, Z.; Morgan, S.; and Prendergast, L. A. 2018. Numerical Coordinate Regression with Convolutional Neural Networks. *CoRR*, abs/1801.07372.

Papandreou, G.; Zhu, T.; Kanazawa, N.; Toshev, A.; Tompson, J.; Bregler, C.; and Murphy, K. 2017. Towards Accurate Multi-person Pose Estimation in the Wild. In *IEEE Conf. Comput. Vis. Pattern Recognit.*, 3711–3719.

Qian, S.; Sun, K.; Wu, W.; Qian, C.; and Jia, J. 2019. Aggregation via Separation: Boosting Facial Landmark Detector With Semi-Supervised Style Translation. In *IEEE Int. Conf. Comput. Vis.*, 10152–10162.

Ronneberger, O.; Fischer, P.; and Brox, T. 2015. U-Net: Convolutional Networks for Biomedical Image Segmentation. In *Medical Image Computing and Computer-Assisted Intervention*, 234–241. Springer.

Russakovsky, O.; Deng, J.; Su, H.; Krause, J.; Satheesh, S.; Ma, S.; Huang, Z.; Karpathy, A.; Khosla, A.; Bernstein, M.; Berg, A. C.; and Fei-Fei, L. 2015. ImageNet Large Scale Visual Recognition Challenge. *International Journal of Computer Vision*, 115(3): 211–252.

Sagonas, C.; Antonakos, E.; Tzimiropoulos, G.; Zafeiriou, S.; and Pantic, M. 2016. 300 Faces In-The-Wild Challenge: database and results. *Image and Vision Computing*, 47: 3–18.

Sun, K.; Xiao, B.; Liu, D.; and Wang, J. 2019. Deep High-Resolution Representation Learning for Human Pose Estimation. In *IEEE Conf. Comput. Vis. Pattern Recognit.*, 5693–5703.

Tai, Y.; Liang, Y.; Liu, X.; Duan, L.; Li, J.; Wang, C.; Huang, F.; and Chen, Y. 2019. Towards Highly Accurate and Stable Face Alignment for High-Resolution Videos. In *Proc. AAAI Conf. Artif. Intell.*, 8893–8900.

Tang, Z.; Peng, X.; Geng, S.; Wu, L.; Zhang, S.; and Metaxas, D. N. 2018. Quantized Densely Connected U-Nets for Efficient Landmark Localization. In *Eur. Conf. Comput. Vis.*, 348–364.

Tu, S.; Dai, Q.; Wu, Z.; Cheng, Z.-Q.; Hu, H.; and Jiang, Y.-G. 2023. Implicit temporal modeling with learnable alignment for video recognition. *arXiv preprint arXiv:2304.10465*.

Wan, J.; Liu, J.; Zhou, J.; Lai, Z.; Shen, L.; Sun, H.; Xiong, P.; and Min, W. 2023. Precise Facial Landmark Detection by Reference Heatmap Transformer. *IEEE Trans. Image Process.*, 32: 1966–1977.

Wang, X.; Bo, L.; and Li, F. 2019. Adaptive Wing Loss for Robust Face Alignment via Heatmap Regression. In *IEEE Int. Conf. Comput. Vis.*, 6970–6980.

Wu, W.; Qian, C.; Yang, S.; Wang, Q.; Cai, Y.; and Zhou, Q. 2018. Look at Boundary: A Boundary-Aware Face Alignment Algorithm. In *IEEE Conf. Comput. Vis. Pattern Recognit.*, 2129–2138.

Xia, J.; Qu, W.; Huang, W.; Zhang, J.; Wang, X.; and Xu, M. 2022. Sparse local patch transformer for robust face alignment and landmarks inherent relation learning. In *IEEE Conf. Comput. Vis. Pattern Recognit.*, 4052–4061.

Zhang, F.; Zhu, X.; Dai, H.; Ye, M.; and Zhu, C. 2020. Distribution-Aware Coordinate Representation for Human Pose Estimation. In *IEEE Conference on Computer Vision and Pattern Recognition*, 7091–7100.

Zhang, J.; Cheng, Z.-Q.; Wu, X.; Li, W.; and Qiao, J.-J. 2022. Crossnet: Boosting crowd counting with localization. In *ACM Int. Conf. Multimedia*, 6436–6444.

Zhou, Y.; Cheng, Z.-Q.; He, J.-Y.; Luo, B.; Geng, Y.; Xie, X.; and Keuper, M. 2023a. Overcoming Topology Agnosticism: Enhancing Skeleton-Based Action Recognition through Redefined Skeletal Topology Awareness. *arXiv preprint arXiv:2305.11468*.

Zhou, Z.; Li, H.; Liu, H.; Wang, N.; Yu, G.; and Ji, R. 2023b. STAR Loss: Reducing Semantic Ambiguity in Facial Landmark Detection. In *IEEE Conf. Comput. Vis. Pattern Recognit.*, 15475–15484.

Zhu, M.; Shi, D.; Zheng, M.; and Sadiq, M. 2019. Robust Facial Landmark Detection via Occlusion-Adaptive Deep Networks. In *IEEE Conf. Comput. Vis. Pattern Recognit.*, 3486–3496.

Zou, X.; Zhong, S.; Yan, L.; Zhao, X.; Zhou, J.; and Wu, Y. 2019. Learning Robust Facial Landmark Detection via Hierarchical Structured Ensemble. In *IEEE Int. Conf. Comput. Vis.*, 141–150.